Industrial Chemistry & Materials

ROYAL SOCIETY OF CHEMISTRY

PAPER

View Article Online
View Journal

Cite this: DOI: 10.1039/d5im00055f

A guideline to optimizing the performance of V_2O_5–MoO_3/TiO_2 catalysts for low-temperature SCR denitrification in industrial application†

Yanchao Qu,[abc] Guangyue Xu,*[bc] Chen Chen,[bc] Jianhua Guo,[bc] Dingjia Liu,[bc] Haiwei Jia,[bc] Haonan Guo,[bc] Shuya Jia,[d] Jiazhen Jia,[bce] Ying Zhang *[a] and Lifeng Yan [a]

The development of novel low-temperature selective catalytic reduction (SCR) denitrification catalysts is a crucial research direction for reducing pollution and carbon emissions. Although V_2O_5–MoO_3/TiO_2 catalysts have been widely used in commercial applications, achieving effective SCR denitrification for low-temperature flue gases remains a significant challenge. In this study, the catalytic efficiency of the catalysts was systematically investigated and optimized by constructing Pearson linear correlation coefficient models between catalytic activity and different pore structures, substrate crystal planes, active site components and properties, *etc.* Through comprehensive characterization and experiments, anatase TiO_2 loaded with 3% V_2O_5 and 10% MoO_3 was developed and demonstrated excellent catalytic activity and stability even in high sulfur content and low-temperature environments. The catalyst was deployed in a pilot plant for over two years, consistently achieving a monthly average denitrification efficiency of over 67% and maintaining an outlet NO_x concentration below 50 mg Nm^{-3}. This study provides a robust and efficient low-temperature catalyst for SCR denitrification and offers valuable insights for future catalyst optimization.

Keywords: Low temperature; SCR denitrification; Sulfur resistance; Structure–activity relationship; Industrial application.

Received 14th April 2025,
Accepted 2nd July 2025

DOI: 10.1039/d5im00055f

rsc.li/icm

1 Introduction

With the rapid development of industry and the increasing stringency of environmental protection regulations, the treatment of pollutants in industrial flue gases has become a pressing issue. Nitrogen oxides (NO_x) are significant air pollutants primarily emitted from coal-fired power plants, industrial furnaces, petrochemical enterprises, motor vehicles, and ship exhausts. These emissions contribute to severe environmental problems, including acid rain and photochemical smog.[1–4]

Selective catalytic reduction (SCR) technology is a widely applied flue gas denitrification technique, typically using NH_3 as a reducing agent to react with NO_x in flue gases to generate non-toxic and pollution-free N_2 and H_2O.[5] The core of this technology is always the denitrification catalyst. Currently, the most widely used commercial catalysts are the V_2O_5–TiO_2 series catalysts, which exhibit good denitrification performance at high temperatures of 300–400 °C, but their application conditions are narrow and stringent.[6] Therefore, the development of SCR denitrification catalysts suitable for low temperatures (usually below 180 °C) is significant for controlling NO_x emissions and improving air quality. More importantly, it can reduce the energy consumption of flue gas treatment and enhance economic benefits.

Industrial flue gases contain a large amount of fly ash and sulfur oxides, which adversely affect the performance and lifespan of denitrification catalysts. Fly ash can block catalyst pores, reduce the active surface area, and cause abrasion to catalysts, thereby decreasing their mechanical and physical lifespan. Sulfur oxides, including SO_2 and SO_3, deactivate catalytic sites through competitive adsorption. Moreover, SO_3 in flue gases containing water reacts with ammonia used for SCR denitrification to form ammonium bisulfate with high

[a] University of Science and Technology of China, No. 96 Jinzhai Road, Hefei, 230026, China. E-mail: zhzhying@ustc.edu.cn
[b] Beijing Nation Power Group Co., Ltd., No. 37 Chaoqian Road, Beijing, 102299, China. E-mail: craneyue@mail.ustc.edu.cn
[c] Zhejiang Kezhuo Environmental Protection Technology Co., Ltd., No. 9 Shiyan Road, Shangyu, 212300, China
[d] University of Strathclyde, James Weir Building, 75 Montrose Street, Glasgow, G1 1XJ, UK
[e] University of Washington, 1410 NE Campus Parkway Seattle, Seattle, WA 98195, USA

† Electronic supplementary information (ESI) available. See DOI: https://doi.org/10.1039/d5im00055f

viscosity. When ammonium bisulfate is deposited on the surface of the catalyst, it reduces the performance of the catalyst and further adsorbs more fly ash, exacerbating pore blockage.[7] Ammonium bisulfate generally begins to decompose at temperatures above 350 °C, and thus the denitrification of low-temperature flue gases imposes stricter requirements on the catalyst's resistance to sulfur and water.

When designing low-temperature catalysts, it is necessary not only to enhance the catalyst's activity at low temperatures, but also to improve the resistance to sulfur and water. It has become the key to the application of low-temperature SCR catalysts in industrial flue gas treatment. In response to this issue, many studies have been conducted, proposing three main solutions: inhibiting the adsorption and oxidation of SO_2,[8–10] constructing competitive adsorption sites,[11] and promoting the decomposition of ammonium bisulfate.[12–14]

Based on these three approaches, previous literature studies have reported on the modification of supports, active centers, and catalyst pore structures. TiO_2 is one of the commonly used supports. It has a large specific surface area and abundant acidic sites, which can enhance catalytic efficiency and protect active centers to improve sulfur resistance.[15] For instance, Li *et al.* investigated the relationship between TiO_2 crystal planes and catalytic activity at low temperatures, and the experimental results showed that the (001) plane has the most excellent performance.[16] Rong *et al.* studied doping rare metals such as Sm, Nd, and Ce on the catalyst that exhibited excellent low-temperature catalytic activity.[17] Referring to desulfurization methods, Tian *et al.* doped Ca in MnO_x/TiO_2 catalysts, protecting the active sites through competitive adsorption of SO_2 and the formation of calcium sulfate.[18] The regulation of catalyst pore structures and physical morphologies improves denitrification activity and stability. For example, Ni *et al.* prepared a three-dimensional ordered mesoporous CeO_2 catalyst substrate loaded with sub-monolayer V_2O_5 and MnO_2 through pore engineering. This catalyst design was conducive to the decomposition of ammonium bisulfate and protected the active sites, exhibiting high activity and sulfur resistance in a wide temperature range.[19] These modification methods have effectively enhanced the low-temperature activity and sulfur resistance of catalysts. However, complex catalyst modifications and the high cost of heteroelement doping increase the cost of catalysts.

V_2O_5–MoO_3/TiO_2 is widely used as low-cost commercial SCR catalyst but suffers from low conversion efficiency and stability at low temperatures.[20,21] In this study, the Pearson linear correlation coefficient strategy was employed to study the structure–activity relationship. The catalytic activity of the catalysts under various reaction conditions (temperature, GHSV, and flue gas composition) was correlated with their physiochemical properties, including the specific surface area, pore volume, pore size, content of active components, V^{4+}/V^{5+} ratio, $Mo^{6-\delta}/Mo^{6+}$ ratio, and oxygen vacancy content. By modulating the catalyst structure, the low-temperature catalytic activity was significantly enhanced. The optimized 3V10Mo/TiO_2 catalyst, after demonstrating stable operation in laboratory for 30 days, was fabricated into a plate-type catalyst and deployed in an industrial flue gas denitrification tower. After over two years of stable operation, the catalyst was characterized and compared with the fresh catalyst, confirming the catalyst's resistance and stability to various components in flue gases under long-term operating conditions in industrial applications.

2 Results and discussion

2.1 Characterization

To explore the relationship between the structure and performance of the catalysts, parameters such as crystal type, grain size, specific surface area, pore volume, pore size, active component (V and Mo) content, and active species ratio (V^{4+}/V^{5+} ratio, $Mo^{6-\delta}/Mo^{6+}$ ratio, and oxygen vacancy content) were investigated systematically.

A series of catalysts with different supports and various contents of V and Mo were synthesized. Currently, most commercially available SCR denitrification catalysts utilize anatase TiO_2 as the support. For comparison, catalysts were also prepared using rutile and mixed-crystal forms of TiO_2 (P25), with V_2O_5 and MoO_3 contents of 3% and 10%, respectively (calculated by the mass fraction of oxides). The catalyst names are listed in Table 1. The anatase, 3V, and 10Mo are the same catalysts. The different names are given to make it easier to compare with other catalysts.

Fig. 1a illustrates the XRD patterns of these three types of catalysts, named rutile, anatase and P25. They exhibited that only the diffraction peaks of TiO_2 were present, with P25 showing diffraction signals for both rutile and anatase structures. No diffraction signals for V and Mo species were detected. This is mainly attributed to two factors: firstly, V and Mo tend to form amorphous species, and secondly, their good dispersion prevents the appearance of long-range ordered diffraction patterns in XRD.

Fig. 1b and c compare a series of catalysts with V_2O_5 loadings ranging from 0 to 4% (while keeping the MoO_3 content

Table 1 Catalyst name and composition

Entry	Catalyst name	Support	Mass fraction[a] (%)	
			V_2O_5	MoO_3
1	Rutile	Rutile TiO_2	3	10
2	Anatase	Anatase TiO_2	3	10
3	P25	P25 TiO_2	3	10
4	0V	Anatase TiO_2	0	10
5	1V	Anatase TiO_2	1	10
6	2V	Anatase TiO_2	2	10
7	3V	Anatase TiO_2	3	10
8	4V	Anatase TiO_2	4	10
9	0Mo	Anatase TiO_2	3	0
10	5Mo	Anatase TiO_2	3	5
11	10Mo	Anatase TiO_2	3	10
12	15Mo	Anatase TiO_2	3	15

[a] The content of all elements is calculated based on the mass fraction of their most stable oxide forms (*e.g.*, V_2O_5, MoO_3), regardless of their actual valence states.

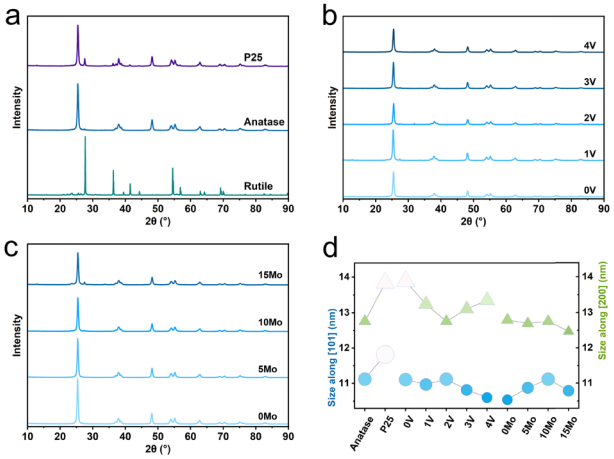

Fig. 1 (a–c) XRD patterns of different catalysts; (d) grain size along the (101) plane and (200) plane.

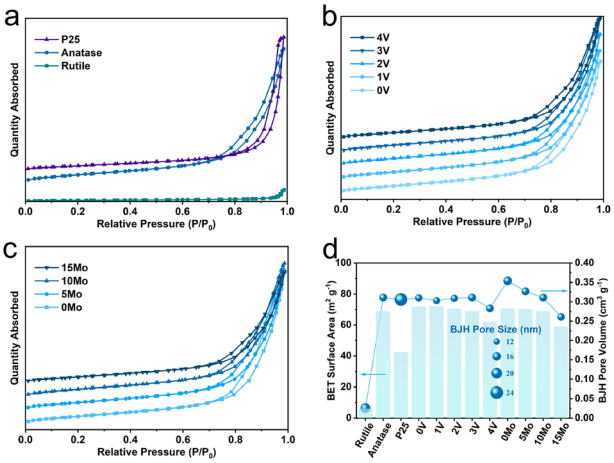

Fig. 2 (a–c) Nitrogen adsorption–desorption curves and (d) BET surface area, BJH pore size, and pore volume of different catalysts.

at 10%, named 0V, 1V, 2V, 3V and 4V) and MoO_3 loadings ranging from 0 to 15% (while keeping the V_2O_5 content at 3%, named 0Mo, 5Mo, 10Mo, and 15Mo). Even loading V_2O_5 or MoO_3 reached as high as 4% or 15%, respectively, no diffraction signals for V and Mo species were observed. A weak diffraction signal for the rutile phase (the (110) plane at 27.5°) was detected when the MoO_3 loading reached 15%. This indicates that excessive Mo doping would lower the phase transformation temperature of TiO_2, causing the original anatase phase to transform into the rutile phase during calcination.

Fig. 1d summarizes the anatase crystal grain sizes calculated by the Scherrer formula, based on the (101) plane at 25.4° and the (200) plane at 48.1°. The grain size of the rutile catalyst along the (101) plane was approximately 45 nm and is not listed in the figure. In Fig. 1d, the blue circles represented the grain size along the (101) plane, which was approximately 10–12 nm; the green triangles represented the grain size along the (200) plane, which was approximately 12–14 nm. It can be seen that the grain sizes of all catalysts were similar. The grain size of P25 TiO_2 was 1 nm larger than that of anatase TiO_2. The doping of V exhibited a volcano-like effect on the grain size along the (101) plane while showing an inverse volcano-like effect on the grain size along the (200) plane. The doping of Mo showed a volcano-like effect on the grain size along the (101) plane and was negatively correlated with the grain size along the (200) plane. These effects might arise from the selective binding of V or Mo species on the different crystal planes of TiO_2 after loading, thereby altering the surface and structural transformation mechanisms of TiO_2 during calcination.

Fig. 2a demonstrates that rutile TiO_2 had a low surface area and lacked pore structures, while anatase TiO_2 possessed a higher surface area and micro/mesopore structures. A higher surface area and more pore structures enhance the dispersion of active species on the surface, thereby improving catalytic activity. Fig. 2b and c show that addition of V or Mo reduces the volume of micropores and mesopores, with Mo having a particularly significant effect on mesopores. In Fig. 2d, the column bars used the left vertical axis, representing the surface area; the lines with symbols used the right vertical axis, representing the pore volume; the size of the symbols represented the different pore sizes. The results showed that anatase had the highest surface area (69 $m^2\ g^{-1}$) and the lowest pore size (14.7 nm). Although P25 had a larger pore size (23.8 nm), its pore volume was similar to that of anatase. This indicates that anatase had more microporous structures and smaller mesoporous structures. Such pore structures have a positive promoting effect on the construction of local mass transfer and reaction environments. The loading of V slightly reduced the surface area and pore volume, while slightly increasing the pore size. This suggests that V was mainly loaded in the smaller pores of TiO_2. The loading of Mo slightly reduced the surface area, pore volume, and pore size. This indicates that Mo was mainly loaded in the larger pores of TiO_2. Larger pores are more likely to be blocked by pollutants such as fly ash or ammonium bisulfate during SCR denitrification.[22] Therefore, V loaded in smaller pores will have better stability for a continuous reaction. Mo loaded in larger pores can effectively promote the decomposition of ammonium bisulfate and improve the catalyst's sulfur resistance.[23]

Fig. 3 shows the SEM and TEM images of three different crystal forms of supports. It can be seen that the particles of rutile TiO_2 were significantly larger, which was consistent with the above analysis of XRD, BET, and BJH. The surfaces of anatase and P25 were both irregularly stacked structures. The particle size of anatase was approximately 60–70 nm, with no standard crystal edges observed in Fig. 3e. Combining the XRD crystal grain size of 11–13 nm, it can be inferred that it formed multiple twin crystal grains. This phenomenon was also observed in P25, but not as distinctly as in anatase. The grain boundaries of twins were often coordinately unsaturated, possessing higher catalytic activity, but they may also be the starting point for catalyst sintering and deactivation.[24] As mentioned in the analysis above, Mo was mainly loaded

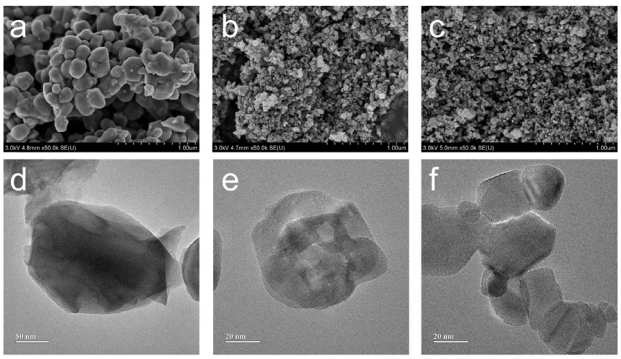

Fig. 3 SEM images of (a) rutile TiO_2, (b) anatase TiO_2 and (c) P25 TiO_2 supported catalysts; and TEM images of (d) rutile TiO_2, (e) anatase TiO_2 and (f) P25 TiO_2 supported catalysts.

in the large pores of TiO_2, including the stacking pores and gaps near the grain boundaries. The morphology of catalysts loaded with different amounts of V and Mo showed no significant differences in SEM and TEM images (Fig. S1†).

XPS was employed to investigate the chemical environments of various elements. Fig. 4a–c present the XPS spectra of V 2p for different catalysts, primarily showing characteristic signals for +5 valence V_2O_5 and +4 valence VO_x. Fig. 4d directly displays the content of V with different valence states (orange bars, using the right vertical axis) and the V^{4+}/V^{5+} ratio (blue line with symbols, using the left vertical axis). V^{4+} is a coordinatively unsaturated V species, predominantly found at the edges and defect sites of V_2O_5. These sites are often locations for bonding with other species, such as V_2O_5–TiO_2. The inter-transformation of V^{4+}/V^{5+} ion pairs provides an electron transfer process, which is a key active site for the SCR reaction. These sites can adsorb and activate NH_3, NO, and O_2.[25]

From Fig. 4a, it can be observed that the catalyst loaded on rutile almost entirely consists of V^{5+} (with a V^{4+}/V^{5+} ratio of only 0.08). This was attributed to the low specific surface area of rutile, leading to poor dispersion of V_2O_5. The V_2O_5 with low dispersion not only had a lower proportion of V^{4+} but also a lower surface V content. Consequently, the catalytic activity was significantly reduced. Among the three types of TiO_2, the catalyst loaded on P25 contained the highest proportion of V^{4+} content, with a V^{4+}/V^{5+} ratio of 0.83. The P25 as a mixed crystal has a larger number of defects and grain boundaries. These sites, after loading V, are more likely to become coordinatively unsaturated, thereby increasing the proportion of V^{4+} content. An increase in the loading amount of V dramatically reduced the proportion of V^{4+}. For catalysts with V loading amounts ranging from 1% to 4%, the V^{4+}/V^{5+} ratios were 2.13, 1.46, 0.68, and 0.49, respectively. Due to increasing the V content, the dispersion of V_2O_5 decreases, the particle size increases, and the number of edge and defect sites also reduces.

The effect of increasing Mo loading on the proportion of V^{4+} content showed a volcano-like trend. A 5% Mo doping increased the V^{4+}/V^{5+} ratio from 0.94 to 1.23, while further increasing to 10% and 15% resulted in a decrease of the V^{4+}/V^{5+} ratio to 0.68 and 0.63, respectively. A small amount of Mo doping improved the loading environment of V, while excessive Mo doping would transfer the oxygen vacancies originally near V to the adjacent region of Mo through an electron transfer effect.[26] Therefore, the content of Mo also needs to be carefully controlled.

Fig. 5 presents the XPS spectra of Mo 3d. Mo primarily existed in the form of +6 valence MoO_3, with a small amount of coordinatively unsaturated $Mo^{6-\delta}$ species also present. In the XPS, $Mo^{6-\delta}$ exhibited a weak and broad peak signal, indicating the possible presence of multiple valence states of low-valent Mo. $Mo^{6-\delta}$ can not only effectively adsorb and activate NH_3, NO, and O_2 to promote the SCR reaction but also reduce the adsorption of sulfur species, thereby enhancing stability.[27] Fig. 5d displays the content of different valence states of Mo (orange bars, using the right vertical axis) and the $Mo^{6-\delta}/Mo^{6+}$ ratio (blue line with symbols, using the left

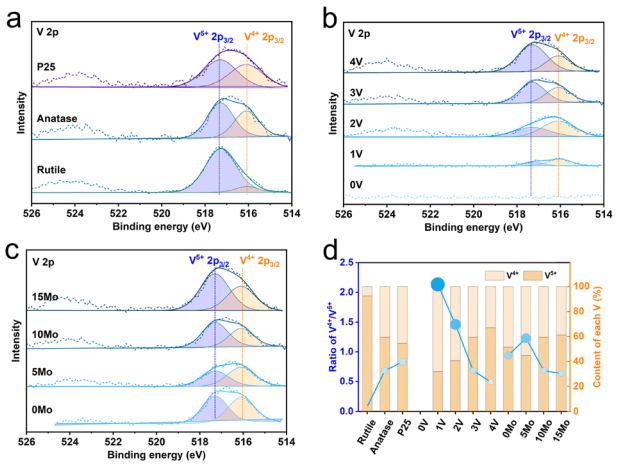

Fig. 4 (a–c) XPS spectra of V 2p and (d) ratio of V^{4+}/V^{5+} and content of each V in different catalysts.

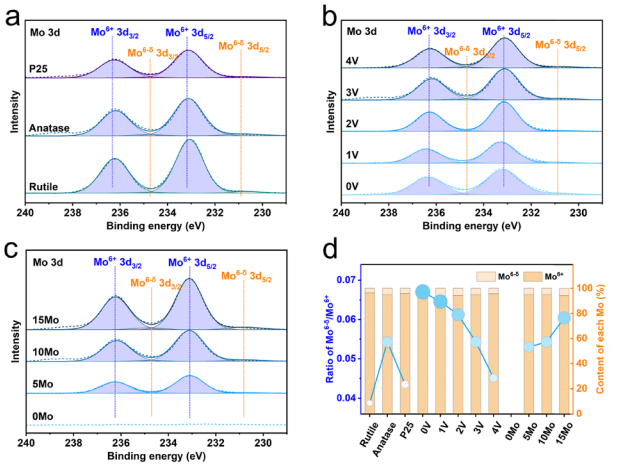

Fig. 5 (a–c) XPS spectra of Mo 3d and (d) ratio of $Mo^{6-\delta}/Mo^{6+}$ and content of each Mo in different catalysts.

vertical axis). For the catalyst supported on anatase, the content of $Mo^{6-\delta}$ was the highest, with a $Mo^{6-\delta}/Mo^{6+}$ ratio reaching 0.054 than those on rutile and P25. The anatase with a smaller pore size exhibited a more significant confinement effect, which had a relatively greater impact on the valence state of Mo. Although rutile also had a small pore size, its low specific surface area made it difficult for loaded Mo to disperse well, thus maintaining the coordinatively saturated form of MoO_3 nanoparticles. The doping of V significantly reduced the content of $Mo^{6-\delta}$ species. With the addition of V_2O_5, from a loading amount of 0% to 4%, the $Mo^{6-\delta}/Mo^{6+}$ ratios were decreased. Different from the impact of V, the increase in Mo doping amount would increase the $Mo^{6-\delta}/Mo^{6+}$ ratio.

Oxygen-deficient sites are widely recognized as key sites for activating molecule oxygen. Fig. 6 shows that the O 1s spectra mainly consisted of three signals: lattice O, chemisorbed O at oxygen vacancy sites, and surface-adsorbed O. Among these, the content of chemisorbed oxygen at oxygen vacancy sites generally represents the content of these vacancy sites.[28] Fig. 6d displays the content of different states of O (orange bars, using the right vertical axis) and the ratio of O-vacancy/(O-vacancy + lattice O) (blue lines with symbols, using the left vertical axis). The rutile catalyst performance was limited by its low specific surface area. The effects of V and Mo loading on oxygen vacancies followed opposite trends. Increasing the V content raised the content of oxygen vacancies, while the Mo loading was the opposite. In addition, the high-valence Mo affected the content of oxygen vacancies near V and Ti.

In summary, from the perspective of physicochemical properties, both anatase TiO_2 and P25 TiO_2 exhibited distinct advantages. Anatase featured the smallest crystal grain size, the highest specific surface area and pore volume, the highest $Mo^{6-\delta}/Mo^{6+}$ ratio, and the highest content of oxygen vacancy ratio, while P25 had the largest pore size and the highest V^{4+}/V^{5+} ratio. In practical applications, the cost of anatase TiO_2 is much lower than P25 TiO_2. Therefore, anatase TiO_2 could be the best choice as the support. The content of V and Mo should be adjusted according to the actual conditions to achieve the best balance between activity and stability.

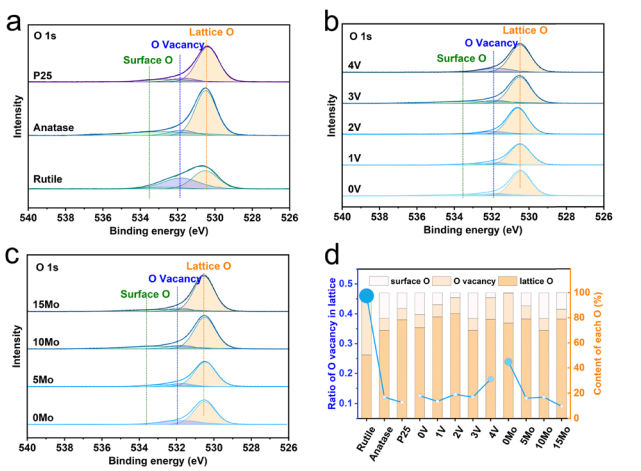

Fig. 6 (a–c) XPS spectra of O 1s and (d) ratio of vacancies in the lattice and content of each O in different catalysts.

2.2 Catalyst testing and optimization

Subsequent activity tests were conducted on the aforementioned catalysts, focusing on the effects of composition, temperature, space velocity, reactant concentration, and pollutant concentration on activity.

Fig. 7a compares the catalytic performance at various temperatures. It can be observed that the catalyst loaded on rutile TiO_2 exhibited lower than 6% NO_x conversion in the range of 150–250 °C. The catalyst loaded on anatase TiO_2 achieved a 34% NO_x conversion at 150 °C, which increased to 75% and 88% at 200 °C and 250 °C, respectively. The catalyst loaded on P25 TiO_2 demonstrated the highest catalytic activity. However, the high cost of P25 limited its large-scale application. Thus, we considered anatase to be the most suitable support for catalysts used in industrial flue gas treatment, and all subsequent tests were conducted with anatase TiO_2 as the support. Fig. 7b exhibits that by loading various amounts of Mo, the reaction activity increased. The Mo loading amount showed a volcano-shaped relationship with reaction activity, reaching the maximum value at 10%. The conclusions for V loading and Mo loading are similar in Fig. 7c. The highest catalytic activity was reached at 150 °C and 250 °C with 3% V loading and 200 °C with 4% V loading. Based on the above data, we believed that V and Mo loading

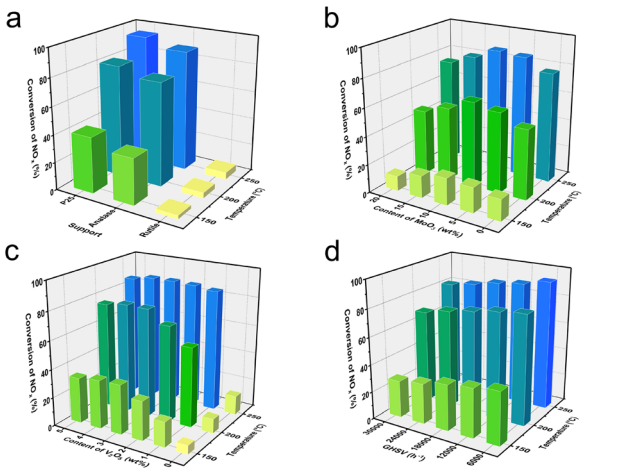

Fig. 7 The SCR reaction using catalysts with different (a) supports, (b) Mo content and (c) V content and (d) different GHSVs at different temperatures. Reaction conditions: 10 mL of catalyst, the total gas flow rate of 3 L min^{-1} containing 700 mg Nm^{-3} of NO, 500 mg Nm^{-3} of SO_2, 10 vol% of water vapor and 4 vol% of O_2 balanced with N_2. The GHSV was generally 18 000 h^{-1} for A–C. The NH_3/NO ratio was always kept to 1. The reactor temperature was precisely maintained using an external heating system at 150, 200, and 250 °C. The catalyst was 3%V_2O_5–10%MoO_3/TiO_2 for D.

amounts of 3% and 10%, respectively, would be the most suitable choices. Subsequent tests used a loading amount of 3% V and 10% Mo. Fig. 7d investigates the changes in reaction efficiency at different space velocities. It can be observed that at different temperatures, the conversion slowly decreased with increasing space velocity. At 200 °C, even with the space velocity increased to 30 000 h^{-1}, the conversion rate still remained at 68%. This indicates that the catalyst had excellent activity over a wide range of flue gas flow rates.

Fig. 8a shows the impact of different oxygen contents on the catalyst. It can be seen that the catalyst had excellent tolerance to extreme oxygen-containing environments. Although the catalytic activity slightly decreased with decreasing oxygen content, it still maintained a high conversion. The catalyst's numerous oxygen vacancies give it a strong ability to activate oxygen, so fluctuations in oxygen concentration within a certain range will not significantly affect the catalyst's activity.[29] Fig. 8b investigates the changes in catalyst activity under different NO_x concentrations. As the NO_x concentration increased from 400 to 900 mg Nm^{-3}, the catalyst's activity slowly decreased. This result indicated that the catalyst maintained high activity over a wide range of NO_x concentrations. Fig. 8c shows the impact of water on the catalyst. Industrial flue gases often contained a certain amount of moisture, which was one of the important factors leading to catalyst poisoning and deactivation. Water had a certain impact on the catalyst's activity, but it was not severe. With the water content of up to 20%, the activity decreased by less than 20%. The influence of water was more significant at low temperatures. This is due to the combined effects of competitive adsorption of water vapor, coverage of the surface by water and ammonium bisulfate, and the erosion of active sites on the catalyst surface by water. Fig. 8d shows the impact of sulfur dioxide.[30] It can be seen that this catalyst had extremely high sulfur resistance. Ordinary SCR denitrification catalysts were easily deactivated by sulfur at low temperatures. This catalyst maintained its original activity without significant deactivation even at a sulfur content as high as 2000 mg Nm^{-3}. On the one hand, this result indicated that the catalyst would be able to operate stably for a long time in flue gases containing sulfur (generally below 35 mg m^{-3}). On the other hand, it showed that the catalyst can withstand short-term high sulfur shock during unexpected situations such as boiler shutdowns and maintenance.

From the above experiments, it can be seen that this catalyst is suitable for flue gas treatment over a wide range of temperatures, space velocities, oxygen contents, and NO_x concentrations, and it has a strong tolerance to water and sulfur.

2.3 Structure–activity relationship

Based on the aforementioned research, we conducted a Pearson linear correlation analysis of the structure–activity relationships, taking into account the physicochemical properties and catalytic activities of the catalysts. The results are presented in Fig. 9.

The correlation analysis employed the Pearson linear correlation analysis. For independent variables X and Y with n samples, the Pearson correlation coefficient r is calculated using the following formula:

$$r = \frac{1}{n-1}\sum_{i=1}^{n}\left(\frac{X_i-\overline{X}}{\sigma_X}\right)\left(\frac{Y_i-\overline{Y}}{\sigma_Y}\right)$$

where X and σ_X are the arithmetic mean value and standard deviation of variable X, respectively, and the same applies to Y.

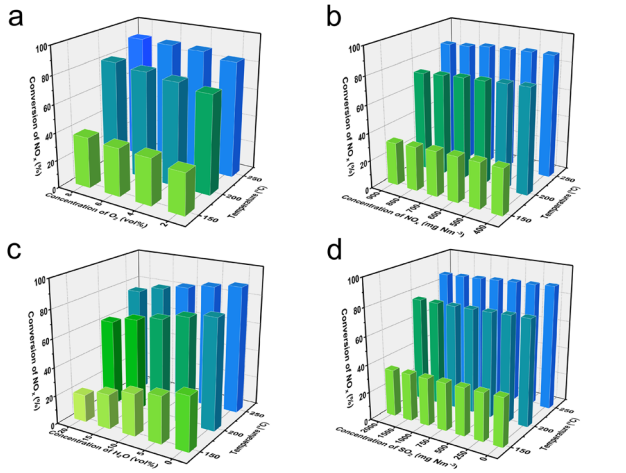

Fig. 8 The SCR reaction using the 3%V_2O_5–10%MoO_3/TiO_2 catalyst with different concentrations of (a) O_2, (b) NO_x, (c) H_2O and (d) SO_2 at different temperatures. General reaction conditions: 10 mL of catalyst, total gas flow rate of 3 L min^{-1} containing 700 mg Nm^{-3} of NO, 500 mg Nm^{-3} of SO_2, 10 vol% of water vapor and 4 vol% of O_2 balanced with N_2. The GHSV was 18 000 h^{-1}. The NH_3/NO ratio was always kept to 1. The reactor temperature was precisely maintained using an external heating system at 150, 200, and 250 °C.

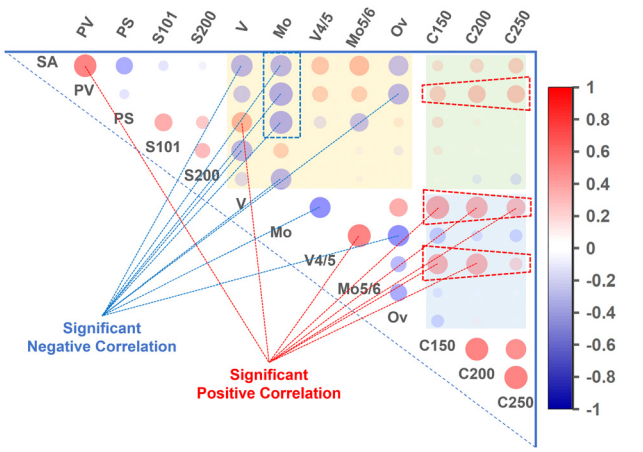

Fig. 9 Pearson linear correlation analysis of physicochemical properties and catalytic activities. SA is the BET specific surface area; PV is the BJH pore volume; PS is the BJH pore size; S101 and S200 are the grain sizes along the (101) and (200) crystal planes, respectively; V and Mo are the mass fractions of the two elements' oxides; V4/5 is the V^{4+}/V^{5+} ratio; Mo5/6 is the $Mo^{6-\delta}/Mo^{6+}$ ratio; O_v is the proportion of oxygen vacancies in the lattice oxygen; and C150, C200, and C250 are the NO_x conversion rates at 150 °C, 200 °C, and 250 °C, respectively.

The Pearson correlation coefficient r represents the degree of linear correlation between two sets of data: $r = 1$ indicates a strong positive linear correlation (represented by red circles in Fig. 9); $r = 0$ indicates no correlation (represented by white areas); $r = -1$ indicates a strong negative linear correlation (represented by blue circles). Deeper colours in Fig. 9 indicate a larger absolute value of r and thus a stronger correlation. The size of the circles also represents the magnitude of the absolute value of r. Given the relatively limited data volume in this study, to enhance the reliability of the analysis results, we set a stricter criterion for strong correlation, considering a correlation coefficient with an absolute value greater than 0.8 as indicative of a significant correlation, indicating a strong linear relationship.

The yellow area in the upper middle of Fig. 9 indicates the correlations between the physical and chemical properties of the catalysts. It can be observed that the content of V is significantly negatively correlated with the specific surface area of the catalyst and significantly positively correlated with the pore size. The content of Mo was significantly negatively correlated with the specific surface area, pore volume, and pore size. This is related to the fact that the loaded components occupied the inner surface of the catalyst support's pores. As discussed above, V is mainly loaded in the smaller pores of the catalyst, thereby somewhat increasing the average pore size. The content of Mo has a noticeable negative impact on the physical surface and pore structure of the catalyst, indicating that the loading amount of Mo should be carefully considered in catalyst design, or further catalyst engineering should be used to improve the loading method of Mo.

Interestingly, the content of V is significantly negatively correlated with the grain size along the (101) crystal plane, while the content of Mo is significantly negatively correlated with the grain size along the (200) crystal plane. This suggested that V and Mo tend to bind near different crystal planes on the surface of TiO_2. This phenomenon provides certain insights for the subsequent microscopic structural design of catalysts. The number of oxygen vacancies is significantly negatively correlated with the pore volume. A smaller pore volume might indicate that more active components are loaded on the inner surface of the pores, thereby increasing the number of oxygen vacancies.

The green area in the upper right of Fig. 9 represents the relationship between physical properties and reaction activity. It can be seen that the pore volume was positively correlated with the activity of the catalyst to a certain extent, and this correlation was more significant at high temperatures. The SCR denitrification reaction is a surface reaction involving multiple molecules, and active sites deep within the pores would be significantly affected by mass transfer resistance and become ineffective. Therefore, a larger pore volume can enhance the activity of the catalyst.

The specific surface area is also positively correlated with the activity of the catalyst, but the significance is not strong. As discussed above, the specific surface area does not represent the area of all reactants accessible to the surfaces. Similarly, it can be found that the pore size has little correlation with the activity of the catalyst, which is determined by the characteristics of the SCR denitrification reaction. Therefore, in catalyst design, pursuing high specific surface area, high pore volume, and large pore size is not the optimal design approach. It is necessary to consider the characteristics of the pore structure and the distribution of active sites comprehensively.

The blue area on the right of Fig. 9 represents the relationship between chemical composition/properties and reaction activity. The content of V was significantly positively correlated with the activity of the catalyst. V is a key active site of the catalyst, so the higher the content of V, the higher the activity of the catalyst. It can also be found that the lower the temperature, the higher the correlation between the content of V and the activity of the catalyst. It can be seen that the V^{4+}/V^{5+} ratio was also significantly positively correlated with reaction activity at low temperatures. In the SCR reaction, the transformation of V^{4+}/V^{5+} ion pairs provided electron transfer, which was a key active site for the SCR reaction. This indicates that when developing SCR catalysts for low-temperature denitrification, increasing the content of V and the V^{4+}/V^{5+} ratio would be a good choice.

The content of Mo showed an insignificant negative correlation with reaction activity, which was consistent with the volcano-shaped curve pattern discussed earlier. An excessively high content of Mo can diminish the catalyst's activity. Concurrently, the $Mo^{6-\delta}/Mo^{6+}$ ratio also showed a weak correlation with reaction activity. Based on the above discussion, the addition of Mo significantly enhanced the catalyst's resistance to sulfur and water, but its catalytic activity promotion was lower than that of V.

In summary, the combination of 3 wt% V and 10 wt% Mo achieves the best balance between activity and stability, representing an ideal choice after considering both structural and electronic properties.

Specifically, a 3 wt% V_2O_5 loading maintains a relatively high V^{4+}/V^{5+} ratio while providing a sufficient number of active sites, thereby achieving the best catalytic activity. The V^{4+}/V^{5+} ratio is significantly positively correlated with reaction activity at low temperatures, indicating that the electron transfer capability of V species is a key active site for the SCR reaction. Moreover, increasing the V content significantly enhances the catalyst's activity, especially at low temperatures.

For Mo, a 10 wt% MoO_3 loading significantly enhances the catalyst's sulfur resistance, thereby significantly extending its service life. Although the Mo content shows an insignificant negative correlation with reaction activity, its role in improving catalyst stability should not be overlooked. The $Mo^{6-\delta}/Mo^{6+}$ ratio also shows a weak correlation with reaction activity, indicating that Mo's primary function is to modulate the electronic structure and acidic sites on the catalyst surface, thereby enhancing its resistance to sulfur.

Mechanistically, the addition of V primarily enhances the catalyst's activity by increasing electron transfer capability (V^{4+}/V^{5+} ratio) and providing more active sites. In contrast, the addition of Mo mainly enhances the catalyst's sulfur and

water resistance by modulating the electronic structure on the catalyst surface.

2.4 Industrial application

Based on the discussion above, it can be found that the catalyst was optimized by improving the pore structure, increasing the content of V, optimizing the chemical environment of V, and regulating the content of Mo. Based on the aforementioned optimized formula, we further added pore-forming agents, binders, and auxiliary materials to increase the mechanical strength, and prepared a plate-type low-temperature denitrification catalyst through roll pressing. This catalyst showed stable performance in a 30 day reaction test in the laboratory, with an average daily denitrification efficiency exceeding 73%, as shown in Fig. 10.

Currently, this catalyst has been in operation for over two years in the denitrification tower of a power plant. The monthly average denitrification efficiency and the NO_x concentration at the outlet of the denitrification tower are shown in Fig. 11. The catalyst maintained a monthly average efficiency of over 67% and a NO_x concentration at the outlet of the denitrification tower consistently below 50 mg Nm^{-3}. The ammonia slip monitoring at the power plant showed that the ammonia slip did not exceed 3 ppm within two years, maintaining good catalytic activity.

Over six months, the average activities of the catalyst were 75%, 74%, 73%, and 70%, respectively, indicating a slow deactivation rate, and it is expected to continue operating for more than 2 years.

The deactivation constant k_D was calculated by the following formula:

$$k_D = \frac{\ln\left(\frac{1-\text{Final Conversion}}{\text{Final Conversion}}\right) - \ln\left(\frac{1-\text{Initial Conversion}}{\text{Initial Conversion}}\right)}{\text{Time}}$$

Based on the continuous operating data, the k_D of this system was 9.45×10^{-5} d^{-1}.

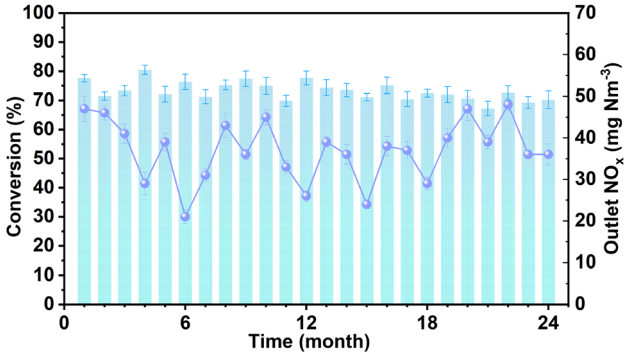

Fig. 11 Industrial application of the plate-type 3%V_2O_5–10%MoO_3/TiO_2 catalyst. Bars: monthly average conversion; line with symbols: concentration of outlet NO_x. For detailed work conditions, see the Experimental section.

During the recent shutdown, we took out a small piece of the catalyst and conducted a series of characterization analyses to investigate the changes in the catalyst after two years of operation. The fresh plate-type catalyst was denoted PC, and the catalyst used for two years was denoted PC-U. Fig. 12a shows the nitrogen adsorption–desorption isotherms of the catalyst. It can be observed that there was a slight change in the shape of the hysteresis loop. The specific surface area has decreased but remains at a high level, without significant surface deactivation caused by the coverage of ammonium bisulfate or ash. The pore volume has slightly increased while the pore size has significantly increased. From the BJH pore size distribution curve in Fig. 12b, it can be seen that the volume of micropores and smaller mesopores below 10 nm has decreased, while the volume of larger mesopores between 10–30 nm has increased. The micropores and smaller mesopores below 10 nm mainly originate from the internal pores and inter-crystalline pores of the catalyst particles, while the mesopores between 10 and 30 nm come from

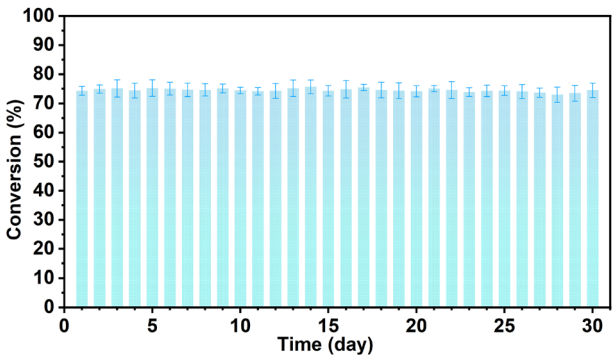

Fig. 10 Lab-scale test for 30 days using the plate-type 3%V_2O_5–10%MoO_3/TiO_2 catalyst. Reaction conditions: 10 mL of catalyst, the total gas flow rate of 3 L min^{-1} containing 700 mg Nm^{-3} of NO, 2000 mg Nm^{-3} of SO_2, 10 vol% of water vapor and 4 vol% of O_2 balanced with N_2. The GHSV was 18 000 h^{-1}. The NH_3/NO ratio was always kept to 1. The reactor temperature was precisely maintained using an external heating system at 200 °C.

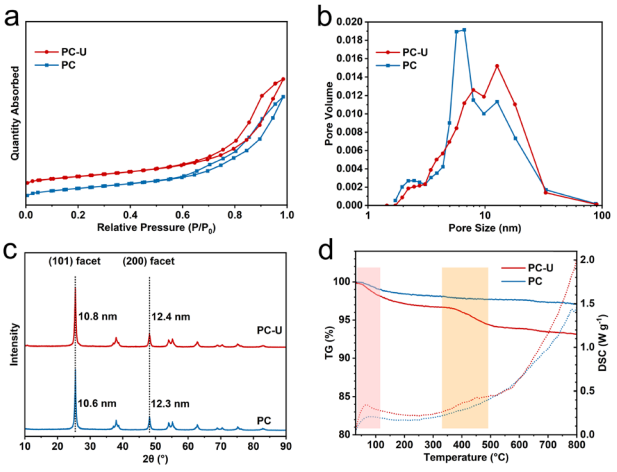

Fig. 12 (a) Nitrogen adsorption–desorption curves; (b) BJH pore volume distribution; (c) XRD patterns; and (d) DSC-TGA curves of fresh (PC) and used (PC-U) industrial applied plate-type catalysts.

the particle stacking. The increase in stacking pores indicated a certain degree of abrasion, contamination, or initial sintering of the catalyst. Fig. 12c shows that the catalyst maintained the anatase crystal phase after the reaction.

Fig. 12d presents the DSC-TG spectra of the catalysts. The weight loss of the fresh catalyst was less than 3%, while that of the used catalyst reached 7%. The two main weight loss temperature ranges are indicated by colored blocks in the figure. The weight loss in the red area below 120 °C mainly comes from the vaporization of water and surface-adsorbed VOCs or volatile inorganic small molecules, while the weight loss in the yellow area around 400 °C mainly comes from the decomposition of surface-deposited ammonium bisulfate.[31] The former indicates that various small-molecule impurities have contaminated the catalyst's surface and pore structure to a certain extent. The latter indicates that a certain amount of ammonium bisulfate has been deposited on the catalyst surface. From the amount of weight loss, the deposition of ammonium bisulfate was about 3–4 wt%. However, no significant deactivation of the catalyst itself was observed. This indicates that ammonium bisulfate has not been attached in large amounts to the active sites of the catalyst, thus maintaining high activity.

Fig. 13 shows the electron microscope images of the catalyst. In Fig. 13a and b, it can be seen that there was significant abrasion on the surface of the catalyst. The originally rough surface with peaks and valleys has become relatively smooth. From the TEM images, it could be seen that the particles have not significantly sintered. Few local regions with a morphology different from the original TiO_2 have been observed. These could be small amounts of pollutants deposited on the catalyst surface.

Fig. 14a shows the chemical composition of the catalyst before and after use, analyzed by XRF. The blue bars represented

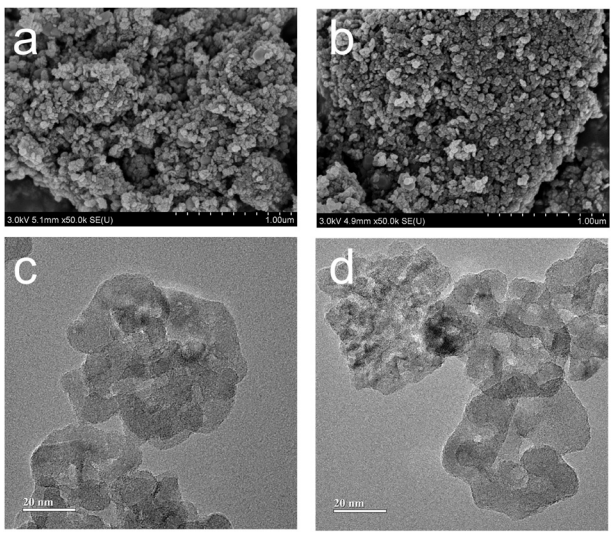

Fig. 13 SEM images of the (a) fresh and (b) used industrial applied plate-type catalysts; TEM images of the (c) fresh and (d) used industrial applied plate-type catalysts.

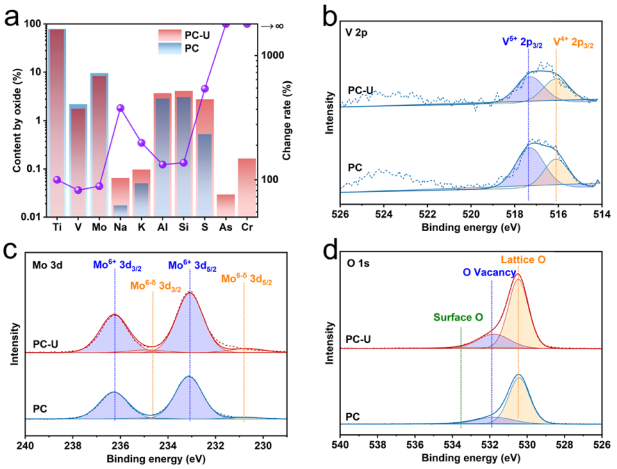

Fig. 14 (a) Elemental content by XRF; and XPS spectra of (b) V 2p, (c) Mo 3d and (d) O 1s of the fresh (PC) and used (PC-U) industrial applied plate-type catalysts.

the elemental content of the fresh catalyst, and the red bars represented the elemental content of the catalyst after the reaction, sharing the left vertical axis; the purple line with symbols represented the change rate of the corresponding elements, using the right vertical axis. Due to the large change rates of some elements, the vertical axis is in logarithmic form for easy reading. After the reaction, the content of V and Mo slightly decreased, but there was no significant loss. The content of Na and K increased significantly (Na_2O: from 0.018% to 0.065%; K_2O: from 0.050% to 0.097%), due to the deposition of alkali metals from the flue gas on the catalyst. The content of Al and Si slightly increased (Al_2O_3: from 2.87% to 3.72%; SiO_2: from 3.08% to 4.12%), indicating that little fly ash had accumulated on the catalyst surface, which was consistent with the on-site catalyst images in Fig. S2.† Although it has been in operation for two years, the catalyst container still looked relatively clean. The plate-type catalyst has a better flow field and is less likely to accumulate dust compared to honeycomb or beaded catalysts.[32] The content of S increased significantly, from the original 0.5% to 2.8%. This is consistent with the 3–4 wt% ammonium bisulfate content given by the thermogravimetric analysis. In the low-temperature flue gas environment, SO_2 is oxidized to SO_3, which then reacts with NH_3 and H_2O to form ammonium bisulfate accumulating in the catalyst over time.[31] In addition, the deposition of two toxic substances, As (0.030%) and Cr (0.164%), was also observed in the catalyst. However, they do not seem to have had a significant impact on the catalyst.

Fig. 14b–d show the XPS spectra of V, Mo, and O. The ratios of V^{4+}/V^{5+}, $Mo^{6-\delta}/Mo^{6+}$, and oxygen vacancies remained essentially unchanged after use, indicating that the active sites of the catalyst have not been physically or chemically poisoned or damaged. Regarding the cost, the industrial application cost of this catalyst is comparable to other commercial catalysts due to the absence of expensive additives or complex preparation processes.

In industrial-scale applications, although there are still issues such as alkali metal contamination, ammonium bisulfate

poisoning, arsenic poisoning, and chromium poisoning, these common poisoning substances do not significantly affect the catalyst's activity. Over the two-year industrial operation, we have been closely monitoring the maintenance and operation conditions and have not yet discovered any situations that would cause significant deactivation of the catalyst.

Contingency plans have been prepared to ensure long-term stable operation, despite the current deactivation and ammonium bisulfate deposition not being severe. Considering that ammonium bisulfate decomposes at high temperatures, a pulsed high-temperature thermal regeneration system will be introduced in future engineering applications. By heating at high temperatures for a short period, ammonium bisulfate can be decomposed to achieve *in situ* catalyst regeneration. Additionally, to address the deposition of alkali metals, ash, and toxic elements, the soot-blowing system will be improved by employing ultrasonic or high-frequency blowing techniques, which can reduce pollutant deposition and extend the catalyst's service life.

It is anticipated that the catalyst may no longer meet the denitrification emission requirements after 3 to 5 years due to decreased activity. In such cases, the catalyst will be replaced, and the used catalyst will be subjected to *ex situ* regeneration processes, such as high-temperature calcination and washing. These measures can not only help restore the catalyst's activity but also promote resource recycling, reducing costs and environmental impacts in industrial applications. Through these strategies, more practical and sustainable solutions will be provided to industrial users.

3 Conclusions

In this study, the V_2O_5–MoO_3/TiO_2 catalyst was applied to the SCR denitrification of low-temperature flue gas. Comprehensive characterization, experiments, and correlation analysis revealed that anatase TiO_2 loaded with 3% V_2O_5 and 10% MoO_3 exhibited superior low-temperature catalytic activity and stability. This catalyst demonstrated robust performance across a wide range of operating conditions, including varying temperatures, space velocities, oxygen contents, and NO_x concentrations. Moreover, it exhibited strong tolerance to water vapor and sulfur compounds.

The study identified several key factors that enhance the catalyst's activity: optimizing the pore structure, increasing the V content, fine-tuning the chemical environment of vanadium, and carefully regulating the Mo content. These modifications collectively contributed to the catalyst's improved performance.

The catalyst has been deployed in an industrial denitrification tower for over two years, consistently achieving a monthly average denitrification efficiency of over 67% and maintaining an outlet NO_x concentration below 50 mg Nm^{-3}. Post-operation characterization revealed some degree of physical abrasion and approximately 3–4% ammonium bisulfate deposition, as well as the accumulation of alkali metals and trace pollutants such as As and Cr. However, the catalyst did not experience significant deactivation and is expected to continue operating effectively.

This study achieved efficient and stable NO_x conversion at low temperatures by modulating the structure of V_2O_5–MoO_3/TiO_2 catalysts. The findings provide valuable insights and guidelines for the further development and optimization of low-temperature SCR catalysts.

4 Experimental

4.1 Materials and equipment

High-purity gases from Shaoxing Fuyuan Special Gas Co., Ltd. were employed in the laboratory experiments: nitrogen (N_2, 99.999%), oxygen (O_2, 99.999%), nitrogen monoxide (NO, 10% balanced by N_2), and sulfur dioxide (SO_2, 10% balanced by N_2). Deionized water was used throughout the experiments.

Analytical grade titanium dioxide (TiO_2, in form of anatase, rutile and P25), ammonium metavanadate (NH_4VO_3), and ammonium heptamolybdate ($(NH_4)_6Mo_7O_{24}$) were obtained from Shanghai Aladdin Biochemical Technology Co., Ltd.

A peristaltic pump (Model: DG12, Baoding Lange Constant Flow Pump Co., Ltd.) was used for fluid handling. A nitrogen oxide analyzer (Model: Thermo Scientific 42i-HL, Thermo Fisher Scientific, U. S.) was employed for gas concentration measurements.

4.2 Catalyst preparation

Typical selective catalytic reduction (SCR) catalyst V_2O_5–MoO_3/TiO_2 was synthesized by an impregnation method. Aqueous solutions of NH_4VO_3 and $(NH_4)_6Mo_7O_{24}$ were added to TiO_2 powder, followed by ultrasonic oscillation for 2 h. Then, the mixture was aged at room temperature for 24 h, dried at 110 °C for 12 h, and calcined at 500 °C for 3 h.

4.3 Catalyst characterization

Thermogravimetric Analysis-Differential Scanning Calorimetry (TGA-DSC) was performed using a NETZSCH STA 449F3 (German) in a N_2 atmosphere using an Al_2O_3 pan.

Powder X-ray diffraction (XRD) was analyzed using a D8 ADVANCE X-ray diffractometer (German). The monochromatized radiation (λ = 1.54056 Å) used was Cu-Kα.

X-ray Fluorescence Spectrometry (XRF) was performed on a ZSX Primus IV (Japan).

The N_2 adsorption–desorption isotherms of the samples were measured at 77 K using an ASAP 2460 (United States). The surface area and pore size distribution of the catalyst were calculated by BET and BJH methods, respectively.

A Hitachi S-4800 (Japan) field emission scanning electron microscope (FE-SEM) and an FEI Tecnai G2 F30 (United States) field emission transmission electronic microscope (FE-TEM) were used to observe the morphology of the catalysts.

X-ray photoelectron spectroscopy (XPS) was conducted on a Thermo Escalab 250Xi spectrometer (United States) equipped with a monochromatic Al Kα X-ray source (1486.6 eV) operating at 150 W.

4.4 Laboratory reaction test

The catalytic reaction experiments were conducted using a self-developed fixed-bed reactor. The catalysts (60–80 mesh) were placed into the pre-heated reactor. The gas mixtures, consisting of NO, SO_2, H_2O, O_2, and N_2, were introduced into the reactor at controlled flow rates using mass flow controllers. In a general test, a total gas flow rate of 3 L min^{-1} containing 700 mg Nm^{-3} of NO, 500 mg Nm^{-3} of SO_2, 10 vol% of water vapor, and 4 vol% of O_2 balanced with N_2 were used. The GHSV was generally 18 000 h^{-1}. The NH_3/NO ratio was always kept to 1. The reactor temperature was precisely maintained using an external heating system at 150, 200, and 250 °C. The long-term test for 30 days used 2000 mg Nm^{-3} of SO_2 at 200 °C. The conversion data were collected manually every hour, with the average and standard deviation of all data points calculated and recorded in Fig. 10.

The gas compositions at the reactor's inlet and outlet were monitored throughout the experiments using an NO analyzer. In all experiments, the catalyst bed was positioned in the center of the reactor, and the gases were mixed in a mixing chamber before entering the reactor. The exhaust gases were treated before being released, ensuring that any remaining pollutants were safely managed.

4.5 Industrial application

The low-temperature SCR catalyst containing 3 wt% of V_2O_5 and 10 wt% of MoO_3 supported on anatase TiO_2 was used in the industrial application in a denitrification tower of a power plant.

The flue gas purification process was: bag filter, low-temperature SCR denitrification, wet desulfurization, electrostatic mist removal and induced draft fan. The low-temperature SCR catalyst was in a flat plate form and was designed in a 3 + 1 layer configuration, with 3 layers initially installed and 1 layer reserved. The designed operating temperature was 190–200 °C. The NO_x content at the inlet of the SCR reactor was 500–800 mg m^{-3}, occasionally reaching above 1300 mg m^{-3}. The actual denitrification temperature of the denitrification reactor was 160–180 °C, with a moisture content of 15–17%. The content of SO_2 was kept below 35 mg Nm^{-3}. The content of O_2 was 4–6 vol%. The GHSV was 10 000 h^{-1}. The SIMS (simultaneous measurement system) online monitoring system was used, which collected 2 data points per second. The average and standard deviations of all data points were then calculated and are shown in Fig. 11.

The fresh plate-type catalyst was denoted PC, while the used catalyst was named PC-U.

Data availability

The data supporting this article have been included in this published article and its ESI† files.

Author contributions

Yanchao Qu: formal analysis, investigation, writing – original draft, conceptualization, funding acquisition, project administration, and writing – review & editing. Guangyue Xu: methodology, conceptualization, writing – original draft, and writing – review & editing. Chen Chen: conceptualization and investigation. Jianhua Guo: methodology, investigation, and funding acquisition. Dingjia Liu: methodology and investigation. Haiwei Jia: formal analysis and investigation. Haonan Guo: investigation and writing – review & editing. Shuya Jia: investigation and writing – review & editing. Jiazhen Jia: investigation and writing – review & editing. Ying Zhang: supervision, funding acquisition, and writing – review & editing. Lifeng Yan: funding acquisition and writing – review & editing.

Conflicts of interest

There are no conflicts to declare.

Acknowledgements

The authors gratefully acknowledge financial support from the National Key R&D Program of China (No. 2023YFA1507500), the National Natural Science Foundation of China (No. 22378377), the Anhui Provincial Major Science and Technology Project (202203a07020018), the Anhui Province Key Scientific Research Projects for Universities (Natural Science) 2022AH051785, and the Ma'anshan City Science and Technology Innovation Tackling Project (2024CSJ001).

References

1 C. Chen, Y. Cao, S. Liu, J. Chen and W. Jia, Review on the latest developments in modified vanadium-titanium-based SCR catalysts, *Chin. J. Catal.*, 2018, **39**, 1347–1365.
2 M. S. Iqbal, Y. Ruam, R. Iftikhar, F. Z. Khan, W. Li, L. Hao, A. W. Robertson, G. Percoco and Z. Sun, Lithium-mediated electrochemical dinitrogen reduction reaction, *Ind. Chem. Mater.*, 2023, **1**, 563–581.
3 S. Liu, J. Gao, W. Xu, Y. Ji, T. Zhu, G. Xu, Z. Zhong and F. Su, Transition metal-based catalysts for selective catalytic reduction of NO by CO: A state-of-the-art review, *Chem. Eng. J.*, 2024, **486**, 150285.
4 S. Jia, L. Wu, L. Xu, X. Sun and B. Han, Multicomponent catalyst design for CO_2/N_2/NO_x electroreduction, *Ind. Chem. Mater.*, 2023, **1**, 93–105.
5 W. Liu, Z. Wang, M. Sun, J. Gao, L. Wang, Z. Gao, Y. Xu, X. Zhao, C. Zhang and L. Yu, Porous washcoat structure in CeO_2 modified Cu-SSZ-13 monolith catalyst for NH_3-SCR with improved catalytic performance, *AIChE J.*, 2022, **68**, e17834.
6 C. Jia, J. Gao, K. W. Huang, V. Jose, P. Thepsithar and J. Lee, Selective catalytic reduction of NO_x in marine engine exhaust gas over supported transition metal oxide catalysts, *Chem. Eng. J.*, 2021, **414**, 128794.
7 C. Liu, H. Wang, Z. Zhang and Q. Liu, The latest research progress of NH_3-SCR in the SO_2 resistance of the catalyst in low temperatures for selective catalytic reduction of NO_x, *Catalysts*, 2020, **10**, 1034.
8 F. Wang, B. Shen, S. Zhu and Z. Wang, Promotion of Fe and Co doped Mn-Ce/TiO_2 catalysts for low temperature NH_3-SCR with SO_2 tolerance, *Fuel*, 2019, **249**, 54–60.

9 W. Tan, A. Liu, S. Xie, Y. Yan, T. E. Shaw, Y. Pu, K. Guo, L. Li, S. Yu, F. Gao, F. Liu and L. Dong, Ce–Si mixed oxide: A high sulfur resistant catalyst in the NH_3–SCR reaction through the mechanism-enhanced process, *Environ. Sci. Technol.*, 2021, **55**, 4017–4026.

10 H. Liu, Z. Fan, C. Sun, S. Yu, S. Feng, W. Chen, D. Chen, C. Tang, F. Gao and L. Dong, Improved activity and significant SO_2 tolerance of samarium modified CeO_2-TiO_2 catalyst for NO selective catalytic reduction with NH_3, *Appl. Catal., B*, 2019, **244**, 671–683.

11 X. Fang, Y. Liu, Y. Cheng and W. Cen, Mechanism of Ce-modified birnessite-MnO_2 in promoting SO_2 poisoning resistance for low-temperature NH_3-SCR, *ACS Catal.*, 2021, **11**, 4125–4135.

12 Y. Chen, C. Li, J. Chen and X. Tang, Self-prevention of well-defined-facet Fe_2O_3/MoO_3 against deposition of ammonium bisulfate in low-temperature NH_3–SCR, *Environ. Sci. Technol.*, 2018, **52**, 11796–11802.

13 K. Guo, Y. Zhu, Z. Yan, A. Liu, X. Du, X. Wang, W. Tan, L. Li, J. Sun, Q. Tong, C. Tang and L. Dong, The dual effects of ammonium bisulfate on the selective catalytic reduction of NO with NH_3 over Fe_2O_3-WO_3 catalyst confined in MCM-41, *Chem. Eng. J.*, 2020, **389**, 124271.

14 Y. Yu, W. Tan, D. An, X. Wang, A. Liu, W. Zou, C. Tang, C. Ge, Q. Tong, J. Sun and L. Dong, Insight into the SO_2 resistance mechanism on γ-Fe_2O_3 catalyst in NH_3-SCR reaction: A collaborated experimental and DFT study, *Appl. Catal., B*, 2021, **281**, 119544.

15 X. Yao, R. Zhao, L. Chen, J. Du, C. Tao, F. Yang and L. Dong, Selective catalytic reduction of NO_x by NH_3 over CeO_2 supported on TiO_2: Comparison of anatase, brookite, and rutile, *Appl. Catal., B*, 2017, **208**, 82–93.

16 Q. Li, X. Li, W. Li, L. Zhong, C. Zhang, Q. Fang and G. Chen, Effect of preferential exposure of anatase TiO_2 {001} facets on the performance of Mn-Ce/TiO_2 catalysts for low-temperature selective catalytic reduction of NO_x with NH_3, *Chem. Eng. J.*, 2019, **369**, 26–34.

17 J. Rong, W. Zhao, W. Luo, K. Kang, L. Long, Y. Chen and X. Yao, Doping effect of rare earth metal ions Sm^{3+}, Nd^{3+} and Ce^{4+} on denitration performance of MnO_x catalyst in low temperature NH_3-SCR reaction, *J. Rare Earths*, 2023, **41**, 1323–1335.

18 Q. Tian, H. Liu, W. Yao, Y. Wang, Y. Liu, Z. Wu, H. Wang and X. Weng, SO_2 poisoning behaviors of Ca-Mn/TiO_2 catalysts for selective catalytic reduction of NO with NH_3 at low temperature, *J. Nanomater.*, 2014, 1–6.

19 K. Ni, Y. Peng, Y. Wang, Z. Huang, H. Zhao, X. Wu and G. Jing, Enhancement of SO_2 resistance on submonolayer V_2O_5–MnO_2/CeO_2 catalyst by three-dimensional ordered mesoporous CeO_2 in low-temperature NH_3–SCR, *Energy Fuels*, 2022, **36**, 2787–2798.

20 K. Wang, B. Lin and W. Xiao, Influence of calcination temperature over vanadium–molybdenum catalysts for the selective catalytic reduction of NO_x with NH_3, *Ind. Eng. Chem. Res.*, 2024, **63**, 5666–5677.

21 Y. Gao, X. Wu, R. Ran, Z. Si, Z. Ma, B. Wang and D. Weng, Effects of MoO_x on dispersion of vanadia and low-temperature NH_3-SCR activity of titania supported catalysts: Liquid acidity and steric hindrance, *Appl. Surf. Sci.*, 2022, **585**, 152710.

22 L. Jin, X. Xie, F. Huang, C. Lu, J. Zhou and Y. Song, Experimental study on the technology of large particle ash interception for SCR De-NO_x equipment, *Electr. Power*, 2018, **51**, 156–161.

23 D. W. Kwon, K. H. Park and S. C. Hong, Enhancement of SCR activity and SO_2 resistance on VO_x/TiO_2 catalyst by addition of molybdenum, *Chem. Eng. J.*, 2016, **284**, 315–324.

24 W. Wu, L. Luo, Z. Li, J. Luo, J. Zhao, M. Wang, X. Ma, S. Hu, Y. Chen, W. Chen, Z. Wang, C. Ma, H. Li and J. Zeng, The importance of sintering-induced grain boundaries in copper catalysis to improve carbon-carbon coupling, *Angew. Chem., Int. Ed.*, 2024, **63**, e202404983.

25 Z. Zhu, Z. Liu, H. Niu, S. Liu, T. Hu, T. Liu and Y. Xie, Mechanism of SO_2 promotion for NO reduction with NH_3 over activated carbon-supported vanadium oxide catalyst, *J. Catal.*, 2001, **197**, 6–16.

26 J. Zhang, L. Chen, Y. Fan, C. Zhao, W. Dai, L. Yang, L. Zhou, J. Zou and X. Luo, Unraveling the high catalytic activity of single atom Mo-doped TiO_2 toward NH_3-SCR: Synergetic roles of Mo as acid sites and oxygen vacancies as oxidation sites, *Chem. Eng. J.*, 2023, **465**, 142759.

27 Y. Chai, G. Zhang, H. He and S. Sun, Theoretical study of the catalytic activity and anti-SO_2 poisoning of a MoO_3/V_2O_5 selective catalytic reduction catalyst, *ACS Omega*, 2020, **5**, 26978–26985.

28 S. Li, Y. Huang, L. Zhao and J. Zhang, Oxygen-functionalized activated carbon supported vanadia catalysts: Unexpected improvement in low-temperature NH_3-SCR performance, *Surf. Interfaces*, 2022, **33**, 102252.

29 B. Zhang, S. Zhang and B. Liu, Effect of oxygen vacancies on ceria catalyst for selective catalytic reduction of NO with NH_3, *Appl. Surf. Sci.*, 2020, **529**, 147068.

30 R. Gui, Q. Yan, T. Xue, Y. Gao, Y. Li, T. Zhu and Q. Wang, The promoting/inhibiting effect of water vapor on the selective catalytic reduction of NO_x, *J. Hazard. Mater.*, 2022, **439**, 129665.

31 C. Zhou, L. Zhang, Y. Deng and S. Ma, Research progress on ammonium bisulfate formation and control in the process of selective catalytic reduction, *Environ. Prog. Sustainable Energy*, 2016, **35**, 1664–1672.

32 W. Wang and W. Li, Analysis and treatment of ash deposition in SCR denitration equipments of W boiler, *Electr. Power*, 2019, **52**, 178–184.